Why Do Model Tropical Cyclones Grow Progressively in Size and Decay in Intensity after Reaching Maturity?

GERARD KILROY AND ROGER K. SMITH

Meteorological Institute, Ludwig-Maximilians University of Munich, Munich, Germany

MICHAEL T. MONTGOMERY

Department of Meteorology, Naval Postgraduate School, Monterey, California

(Manuscript received 12 June 2015, in final form 17 August 2015)

ABSTRACT

The long-term behavior of tropical cyclones in the prototype problem for cyclone intensification on an f plane is examined using a nonhydrostatic, three-dimensional numerical model. After reaching a mature intensity, the model storms progressively decay while both the inner-core size, characterized by the radius of the eyewall, and the size of the outer circulation—measured, for example, by the radius of the gale-force winds—progressively increase. This behavior is explained in terms of a boundary layer control mechanism in which the expansion of the swirling wind in the lower troposphere leads through boundary layer dynamics to an increase in the radii of forced eyewall ascent as well as to a reduction in the maximum tangential wind speed in the layer. These changes are accompanied by changes in the radial and vertical distribution of diabatic heating. As long as the aggregate effects of inner-core convection, characterized by the distribution of diabatic heating, are able to draw absolute angular momentum surfaces inward, the outer circulation will continue to expand. The quantitative effects of latitude on the foregoing processes are investigated also. The study provides new insight into the factors controlling the evolution of the size and intensity of a tropical cyclone. It provides also a plausible, and arguably simpler, explanation for the expansion of the inner core of Hurricane Isabel (2003) and Typhoon Megi (2010) than that given previously.

1. Introduction

When measured by the extent of gale-force winds (wind speeds exceeding 17 m s^{-1}), tropical cyclones are observed to possess a wide range of sizes from large Pacific typhoons with gale-force winds extending beyond 1000 km from their center to midget storms with a radius of gales no more than about 50 km. There is a large variation also in the size of the eye, which is not necessarily related to the extent of gales. Examples of such extreme sizes include at the large end Supertyphoon Tip (1979), which occurred in the western North Pacific (Dunnavan and Diercks 1980), and Hurricane Sandy (2012), which caused widespread damage along the eastern seaboard of the United States (e.g., Lussier et al. 2015). An example at the small end is Tropical Cyclone Tracy (1974), which devastated the Australian city of Darwin on Christmas Day (Davidson 2010 and references therein). The radius of gales in the case of Tracy was merely 50 km, less than the size of the eye in Tip, where gales were spread over an 1100-km radius. Thus, Tip had an area about 400 times larger than that of Tracy. In contrast, Hurricane Wilma (2005) was a case with a broad tangential circulation but a pinhole-sized eye (Beven et al. 2008).

In a climatological study of tropical cyclone size, Merrill (1984) showed that tropical cyclones of the western North Pacific are characteristically twice as large as their Atlantic counterparts and that the typical size of tropical cyclones varies seasonally and regionally and is only weakly correlated with cyclone intensity (as measured by the maximum surface wind or minimum surface pressure). He noted that, within a single season, tropical cyclones come in all sizes and attain a variety of intensities. A more recent climatological study

Corresponding author address: Dr. Gerard Kilroy, Meteorological Institute, Ludwig-Maximilians University of Munich, Theresienstr. 37, 80333 Munich, Germany.
E-mail: gerard.kilroy@lmu.de

DOI: 10.1175/JAS-D-15-0157.1

of tropical cyclone size by Dean et al. (2009) showed that the size distribution of Atlantic tropical cyclones was lognormal.[1]

Although there has been a number of theoretical studies examining factors that determine tropical cyclone size (e.g., Yamasaki 1968; Rotunno and Emanuel 1987; DeMaria and Pickle 1988; Smith et al. 2011; Rappin et al. 2011; Hakim 2011; Li et al. 2012; Chavas and Emanuel 2014), there remain some basic issues to be resolved. For example, an underlying assumption of all of these studies is that there exists a global quasi-steady solution for storms, an assumption that would require, inter alia, that the storm environment be quasi steady. However, the existence globally of a realistic, quasi-steady state even when the environment is quiescent, has been questioned on the grounds of both angular momentum and thermodynamic considerations (Smith et al. 2014), raising the likelihood that both the size and intensity of the storm evolve progressively with time. In fact, according to the conventional paradigm for tropical cyclone intensification (see Montgomery and Smith 2014 and references therein), one would anticipate that the outer circulation will expand as long as the aggregate effect of deep convection [including the eyewall and convective rainbands (Fudeyasu and Wang 2011)] remains strong enough to maintain the inward migration of absolute angular momentum surfaces. If this is the case, the broadening circulation would have consequences for the boundary layer dynamics, which play a role in determining the radii at which air ascends into the eyewall and the maximum tangential wind speed, which has been shown to occur in the boundary layer (e.g., Kepert 2006a,b; Montgomery et al. 2006, 2014; Bell and Montgomery 2008; Sanger et al. 2014).

Xu and Wang (2010) suggested that a broadening of the circulation would increase also the surface moisture flux outside the eyewall, thereby increasing the ''convective activity'' at these radii and enhancing the radial inflow beyond these radii. While at first sight this argument may seem reasonable, it is important to quantify the link between the increase in convective activity as a result of moistening. Presumably, convective activity is characterized by the convective mass flux and its variation with radius.

In two recent papers, Chan and Chan (2015) and Frisius (2015) carried out a series of idealized numerical simulations of tropical cyclones with a view to exploring the controls on storm size. Chan and Chan (2015, p. 2235) sought ''to *understand:* [emphasis added] how the initial size ... and planetary vorticity ... influence TC [tropical cyclone] size change.'' They defined the size as the radius of the azimuthally averaged wind speed of $17\,m\,s^{-1}$ at a height of 10 m. An understanding of size using this definition requires a consideration of frictional effects, but this was not done. Instead, size differences were explained mostly in terms of differences in inertial stability, the relevance of which is questionable in the friction layer.[2] In addition, they did not mention the differences in the strength of the convective forcing, which, as we will show here, are fundamental to understanding these effects. Indeed, Smith et al. (2015, hereafter SKM) showed that the convective forcing is paramount and that inertial stability (above the boundary layer) plays a relatively minor role, certainly on the intensification at different latitudes. They showed also that the boundary layer has a strong control on the location and strength of the convective forcing as the latitude is varied.

A significant finding of Frisius (2015), who used an axisymmetric model, was that, even in a quiescent environment, a steady-state solution of the model requires an artificial (and therefore unrealistic) source of absolute angular momentum to maintain the angular momentum lost by the frictional torque near the surface where the flow is cyclonic. When this source was suppressed, the upper anticyclone descended to the surface, where cyclonic relative angular momentum can be diffused into the system. Both these results are in accordance with the theoretical predictions of Smith et al. (2014). Frisius (2015, p. 14) conceded that his steady-state solutions, which took many months to achieve, were not relevant to understanding size in realistic storms, which are intrinsically unsteady.

Chavas and Emanuel (2014) used extended time integrations of an axisymmetric model to examine the size of tropical cyclones in a state of statistical equilibrium. They found that the size scales linearly with potential intensity divided by the Coriolis parameter. Like Frisius, Chavas and Emanuel (2014, p. 1678) conceded that ''the extent to which these equilibrium results can be applied to real storms in nature is not clear,'' and they explain the reasons why: ''the time scales to equilibrium

[1] The metric for size used by Dean et al. (2009, p. 1) was ''the radius of vanishing storm winds normalized by the theoretical upper bound for this radius given by the ratio of the potential intensity to the Coriolis parameter.'' The radius of vanishing storm winds was inferred from the estimated radius of gale-force winds using Emanuel's (2004) revised steady-state hurricane model.

[2] The point is that inertial stability is normally judged by considering the forces on an air parcel that is subjected to a small radial displacement in a swirling flow in gradient wind balance. Such an analysis is meaningless in the boundary layer, where gradient wind balance is not satisfied and where, at outer radii, the agradient force is negative.

identified here for the control simulation are significantly longer than the lifespan of tropical cyclones on Earth,'' and ''storms in nature rarely exist in a truly quasi-steady environment for more than a couple of days, if at all.''

We acknowledge the challenges of understanding size change but do not subscribe to the statement on the first page of Frisius (2015) that ''little is known about the mechanism controlling [tropical cyclone] size.'' Nevertheless, we think that there is scope for improving an understanding of the interplay of processes that must be of prime importance and such is the motivation of the present paper. Any improvement would have obvious benefits for forecasters, if only in improving their ability to interpret model behavior, on which all modern forecasts are based.

The present paper builds on the studies of Smith et al. (2014) and SKM. These focused on the prototype problem for tropical cyclone intensification, which considers the evolution of a prescribed, initially cloud-free axisymmetric vortex in a quiescent environment on an f plane. The first of these studies sought to understand the lack of a steady state in the 30-day simulation, while the second sought to understand why low-latitude storms intensify more rapidly than those at higher latitudes, all other factors being the same. Here we use the same three-dimensional numerical model as SKM to understand the long-term behavior of the vortex (on the time scale of a month) and the effects of latitude on this evolution.

The paper is organized as follows. In section 2 we present the configuration of the numerical model; then in section 3 we discuss the results of the calculations. In section 4 we provide physical interpretations of the model behavior. In section 5 we offer an alternative explanation for size expansion in two notable tropical cyclones. In section 6 we discuss the latitudinal dependence of the calculations. The conclusions are given in section 7.

2. The numerical model

The numerical experiments use a modified version of the Fifth-generation Pennsylvania State University–National Center for Atmospheric Research Mesoscale Model (MM5) and are with a few exceptions identical to those described by SKM (see their section 2). A detailed description of the MM5 can be found in Grell et al. (1995). The model is configured here with three domains: a coarse mesh of 45-km grid spacing and two, two-way nested domains of 15- and 5-km grid spacing, respectively. The domains are square and are 9000, 4500, and 1500 km on each side. The model has 24 sigma levels in the vertical, 7 of which are below 850 hPa to provide adequate vertical resolution of the boundary layer. A key difference between the model configuration here and that used by SKM is the application of Newtonian relaxation to the temperature field with a time scale of 10 days (Mapes and Zuidema 1996).

The initial vortex is axisymmetric with a maximum tangential wind speed of $15\,\mathrm{m\,s^{-1}}$ at the surface at a radius of 100 km. The magnitude of the tangential wind decreases sinusoidally with height, vanishing at the top model level. The temperature field is initialized to be in thermal wind balance with the wind field using the method described by Smith (2006). The far-field temperature and humidity are based on the neutral sounding of Rotunno and Emanuel (1987). The sea surface temperature is a constant (27°C).

Three calculations are performed on an f plane centered at latitudes 10°, 20°, and 30°N. The simulations are carried out for 30 days with data output every 15 min. As the simulations run for 30 days, the latent and sensible heat fluxes are switched off beyond a radius of 500 km as a precaution to avoid excessive low-level moistening of the far-field environment. This is another difference to the calculations in SKM.

3. Results: Vortex evolution

The early evolution of the model cyclone is the same as that described in Nguyen et al. (2008). In brief, the imposition of surface friction from the initial instant leads to the formation of a surface-based boundary layer with inflow near the surface, ascent inside the radius of maximum tangential wind speed, and outflow in a shallow layer above the inflow layer. The inflow progressively moistens through surface moisture fluxes and, after about 10 h, some of the ascending air reaches its level of free convection and cells of deep convection develop. At first, a regular pattern of convective updrafts form in an annular region inside the initial radius of the maximum tangential wind speed, but the pattern progressively loses any degree of symmetry, a reflection of the stochastic nature of deep convection and the number of updrafts declines. The updrafts rotate cyclonically around the vortex center and have lifetimes on the order of an hour. As they develop, they tilt and stretch the local vorticity field and an approximate ringlike structure of intense, small-scale, vorticity dipoles emerges. The dipoles are highly asymmetric in strength with strong cyclonic vorticity anomalies and much weaker anticyclonic vorticity anomalies.

The development of the updrafts heralds a period lasting about 3–6 days during which the vortex intensifies rapidly. Eventually, the maximum azimuthally averaged tangential wind speed $V_{\max}$ reaches a

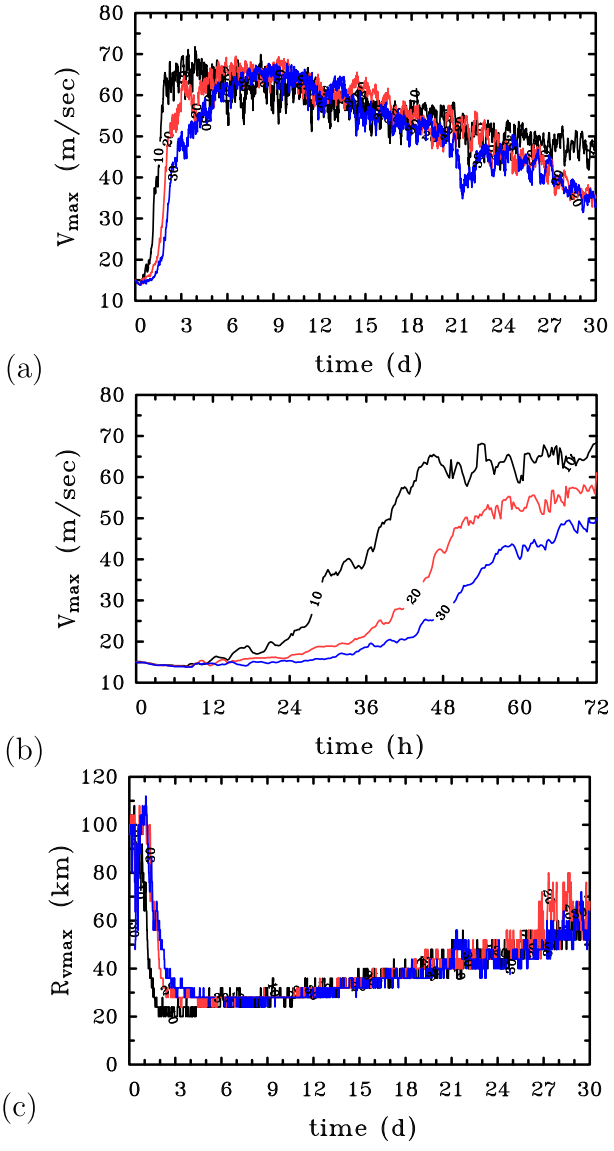

FIG. 1. Time series of azimuthally averaged quantities at latitudes 10°, 20°, and 30°N: maximum tangential wind speed V_{max} during (a) the entire 30-day calculation and (b) the first 3 days, which encompasses the intensification phase. (c) The radius at which the maximum tangential wind speed occurs R_{vmax}.

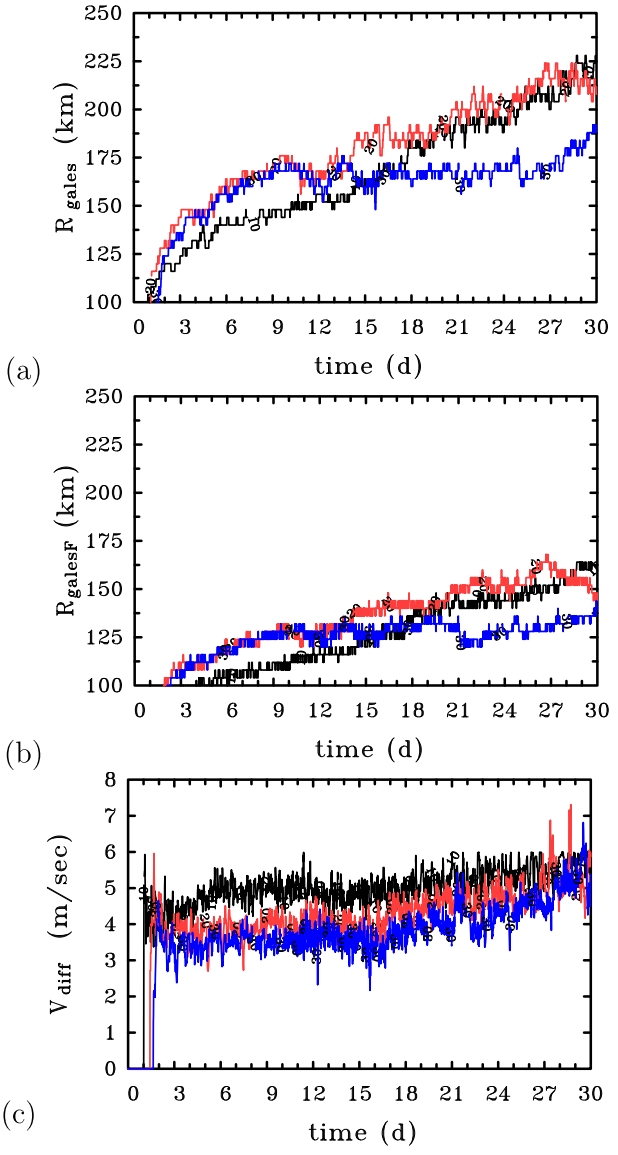

FIG. 2. Time series of azimuthally averaged quantities at latitudes 10°, 20°, and 30°N: (a) the radius at which gale-force winds occur R_{gales}, where R_{gales} is calculated at a height of 1 km and corresponds to the radius of 17 m s^{-1} tangential winds outside the eyewall; (b) the radius at which gale-force winds occur R_{galesF}, where R_{galesF} is calculated at a height of 10 m and corresponds to the radius of 17 m s^{-1} total winds outside the eyewall; (c) the difference between the tangential wind at a height of 1 km and the total wind at R_{galesF} at a height of 10 m at this radius.

quasi-steady state. However, in terms of other metrics, this quasi-steady state is an illusion, and other quantities such as the strength of the upper anticyclone and the radius of gales are still evolving (see, e.g., Smith et al. 2014).

The longer-term behavior of the vortex is summarized in Figs. 1 and 2.

a. Intensity and inner-core size

Figure 1 shows time series of V_{max} over long and short time periods together with the radius R_{vmax} at which V_{max} occurs in the three calculations for different latitudes. These quantities can be at any height, but are typically at a few hundred meters above the surface, within the inflow layer. In terms of V_{max}, the vortex in all three simulations undergoes an intensification phase lasting about 3–6 days, followed by a quasi-steady state that lasts up to about 6 days. All three vortices have a

similar V_{max} during the mature phase. From day 9 onward, the vortices progressively decay and the decay rate is weaker in the 10°N simulation (Fig. 1a). At the end of the simulation, V_{max} in the 10°N experiment has decreased by about 20 m s^{-1} from its maximum value, while that in the 30°N experiment has decreased by about 35 m s^{-1}.

Initially R_{vmax} is located at a radius of 100 km but contracts to about 20–30 km after 3 days. The most rapid contraction occurs during the rapid intensification phase, where absolute angular momentum surfaces are drawn inward quickly within and above the boundary layer. During the most intense phase (between about 3 and 9 days), R_{vmax} is essentially the same in all three simulations, but it fluctuates more at 20°N during the decay phase (Fig. 1c).

b. Outer-core size

The outer-core size is characterized by the outermost radius of gale-force winds R_{gales}, defined here as the radius of 17 m s^{-1} tangential winds at a height of 1 km, which is approximately at the top of the boundary layer. Forecasters are interested in the radius of gales, say R_{galesF}, defined as the (outer) radius at which the total wind speed at a height of 10 m is 17 m s^{-1}. However, from a theoretical viewpoint, a definition based on the tangential wind component just above the top of the boundary layer is a preferable measure of size, as this radius is related to absolute angular momentum at R_{gales} [i.e., $M_{gales} = 17 \times R_{gales} + (1/2)fR^2_{gales}$]. Moreover, above the boundary layer, where frictional effects can be neglected, absolute angular momentum is materially conserved to a good approximation (i.e., $\partial M/\partial t = -\mathbf{u}_s \cdot \nabla M$), where $\mathbf{u}_s$ is the velocity vector in a vertical plane that characterizes the secondary circulation. In other words, a spinup of the tangential wind requires a component of flow normal to the M surfaces toward lower M.

Above the boundary layer in an inertially stable warm-cored vortex, $\partial M/\partial r > 0$ and $\partial M/\partial z < 0$ so that ∇M points downward and outward. It follows that the radius of gales above the boundary layer will always expand if the foregoing condition is satisfied. Clearly, the magnitude of $\mathbf{u}_s$ will be determined, inter alia, by some measure of the strength and radial distribution of the convective forcing, which, in turn, will depend on both the boundary layer dynamics and thermodynamics. It may depend also on the inertial stability above the boundary layer.

Within the boundary layer, the absolute angular momentum of an air parcel is reduced by friction. Thus, friction needs to be considered when calculating the radial movement of the M surfaces to determine whether the radius of gales increases or not. It follows that if one uses R_{galesF} to measure size, one cannot ignore frictional effects in any explanation of size changes. Moreover, since R_{galesF} is based on the total wind speed at a height of 10 m, the radial momentum equation must be considered in any analysis of its behavior.

As the latitude increases, so does the radial gradient of absolute angular momentum, but the implied increase in the inertial stability and any decrease in the strength of convective forcing (see below), may reduce the strength of the secondary circulation. Therefore, the net effect on the radial displacement of the M surfaces and hence on the spinup rate cannot be anticipated and must be calculated. Figure 2 shows time series of R_{gales}, R_{galesF}, and the difference between the total winds at the surface (17 m s^{-1}) at R_{galesF} and the tangential wind component at a height of 1 km. As shown in Figs. 2a and 2b, the outer-core size of the vortices at 10° and 20°N grows continuously, with the most rapid growth occurring during the intensification phase. At 30°N the vortex size remains relatively constant during the decay phase until the final days of the simulation, suggesting that deep convection in the weakening system becomes progressively unable to draw in M surfaces in the far field. Despite the larger background rotation rate at higher latitudes, the 30°N vortex is the smallest in size from day 15 onward. The 20°N vortex becomes the largest in size after about 14 days, and it continues to grow in size until the end of the simulation, suggesting that $-\mathbf{u}_s \cdot \nabla M$ remains positive at R_{gales}, even though the inner-core intensity of the vortex is decreasing. In the final 2 days, the 10°N vortex becomes the largest in size, despite spending the initial 15 days as the smallest.

A comparison of Figs. 2a and 2b shows that the evolution of storm size based on R_{galesF} is similar to that based on R_{gales}, although R_{gales} always exceeds the value of R_{galesF} at all three latitudes. Typically, R_{gales} is about 25 km larger than R_{galesF} during the mature phase, and the difference increases to values as large as 60 km in the decay phase at all three latitudes. Moreover, at R_{galesF}, the tangential wind speed at a height of 1 km exceeds the total surface wind speed by between 3 and 5 m s^{-1} with a noticeable dependence on latitude (Fig. 2c).

An alternative depiction of the vortex evolution is provided by the Hovmöller diagram of the azimuthally averaged tangential wind component near the top of the boundary layer (Fig. 5), taken nominally at a height of 1 km with the radius of the wind maximum and radius of gales at this level indicated. To suppress small-scale noise and highlight the main features, the field has been smoothed by computing a 3-h time average centered on times 12 h apart. This figure shows also the progressive expansion of the inner and outer core as the vortex matures and decays and will prove useful in the discussion of the boundary layer behavior in section 4a.

c. Relationship to Smith et al. (2011)

The foregoing results have some similarities to those from the axisymmetric calculations in Smith et al. (2011), which were designed to investigate the rotational constraint on the intensity and size of tropical cyclones using a minimal, three-layer, axisymmetric model. For example, the vortices in the three simulations shown here have a similar maximum intensity during their mature phases as do those in this range of latitudes in Smith et al. (2011). Moreover, during the mature phase in the calculations here, the storm at 20°N is larger than those at 10° and 30°N, which is similar also to the findings of Smith et al. (2011). However, a problem with such comparisons is that the vortices in the Smith et al. calculations reached a quasi-steady state after a few days, whereas those in the present study ultimately decay in terms of V_{max} at rates that are dependent on latitude. Thus, after 30 days, V_{max} at 10°N is appreciably larger than that at 30°N, and the sizes of the vortices are still increasing. As shown by Smith et al. (2014), the existence of a steady state requires the presence of a steady angular momentum source in the model that will not be present in real storms.

d. Secondary circulation

The strength of the secondary circulation depends, inter alia, on the strength and radial location of the convective forcing, which are controlled by the dynamics of the boundary layer. Measures of this strength and location are the maximum azimuthally averaged vertical velocity w_{max} and the radius R_{wmax} at which it occurs. The long-term behavior of these quantities is shown in Fig. 3. The largest w_{max} occurs at the lowest latitude during the intensification phase, as shown in SKM, although during the 30-day integration, w_{max} is similar at all latitudes. At 20° and 30°N, the largest values of w_{max} occur in the mature phase, and R_{wmax} changes little during this period. Subsequently, w_{max} decreases at all three latitudes, and R_{wmax} moves radially outward with time, the radial increase decreasing with increasing latitude.

A complementary measure of the strength of the azimuthally averaged secondary circulation is the vertical mass flux carried by the circulation in the eyewall updraft. This quantity characterizes the ability of the eyewall updraft to ventilate the mass flux expelled by the inner-core boundary layer. If not all of the mass ejected from the boundary layer can be accepted by eyewall updraft, the residual will flow radially outward, leading to spindown of the tangential wind above the boundary layer as a result of absolute angular momentum conservation. Figure 4 shows a time series of vertical mass

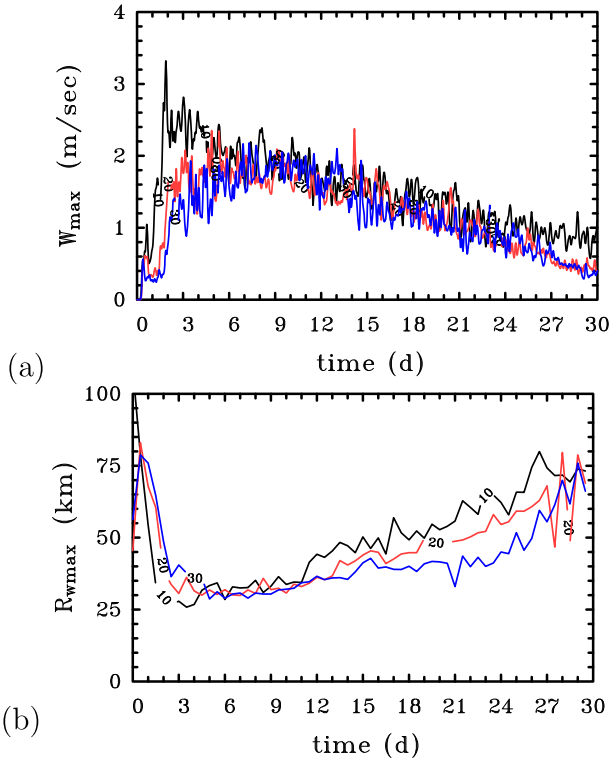

FIG. 3. Time series of azimuthally averaged quantities at latitudes 10°, 20°, and 30°N: (a) azimuthally averaged maximum vertical velocity; (b) azimuthally averaged, 12-h time-averaged radius at which the maximum vertical velocity at a height of 6 km occurs.

flux at heights of 1.5 (Fig. 4a) and 6 km (Fig. 4b), calculated by integrating the vertical mass flux where it is positive radially out to 200 km. The largest mass flux at both these heights occurs at the lowest latitude throughout the 30-day integration. Interestingly, the mass flux at 10°N continues to increase during the decay phase. Thus, even though the eyewall expands and w_{max} decreases with time, the amount of mass being carried by the updraft at a height of 6 km increases at this latitude. The dependence of these time series on latitude will be discussed further in section 6.

e. Summary

In summary, the model cyclones grow progressively in size and decay in intensity after reaching their mature stage. In terms of either R_{gales} or R_{galesF}, the vortex size increases with time throughout the calculation, except at the largest latitude, where it tends to become steady. The strongest vertical motion occurs during the intensification phase and weakens with time, while the location of the strongest vertical motion moves radially outward with time at all latitudes studied. The evolution of vertical mass flux carried by the eyewall updraft

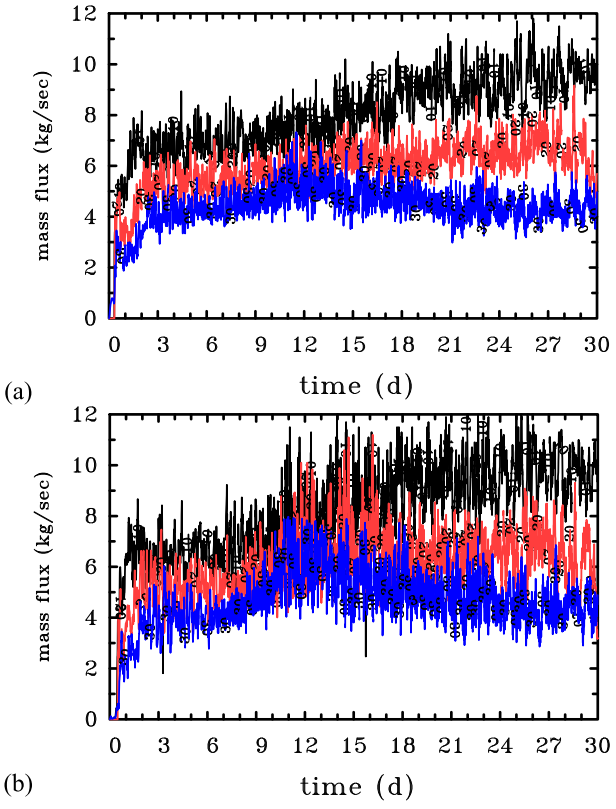

FIG. 4. Time series of azimuthally averaged radially integrated mass flux at latitudes 10°, 20°, and 30°N at heights of (a) 1.5 and (b) 6 km. This quantity is calculated by integrating the vertical mass flux, where it is positive, radially out to 200 km and then dividing by 1×10^9 for plotting purposes.

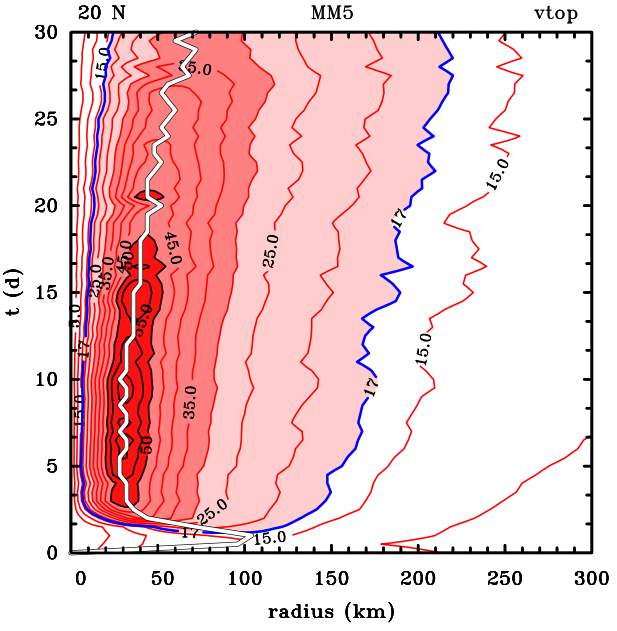

FIG. 5. Azimuthally averaged and temporally smoothed Hovmöller plot of tangential velocity at a height of 1 km near the top of the boundary layer from MM5 output at 20°N. Contour intervals are as follows: Contours are every 5 m s^{-1}. The 17 m s^{-1} contour representing the radius of gales is colored blue. The interval from 17 to 30 m s^{-1} is shaded light red, that from 30 to 50 m s^{-1} is shaded slightly darker red, and values of 50 m s^{-1} and above are shaded dark red with black contours. The white curve represents the radius of the time and azimuthally averaged maximum tangential velocity at a height of 1 km, while the outer blue contour represents the time and azimuthally averaged radius of gales at this height.

depends also on latitude. We explore the reasons for these findings in section 6.

4. Physical interpretations

The tight coupling between the flow above the boundary layer and that within the boundary layer makes it impossible, in general, to present simple cause and effect arguments to explain vortex behavior. The best one can do is attempt to articulate the individual elements of the coupling, which might be described as a set of coupled mechanisms. In this spirit, we begin in the next subsection by examining the role of the expanding outer wind profile on the flow within the boundary layer, isolating what we refer to as a boundary layer control mechanism. Then, in sections 4b and 4c, we articulate the series of mechanisms that are involved in providing boundary layer feedback to the interior flow.

a. The boundary layer control mechanism

To explore the behavior of the outer-core expansion of the vortices described in section 3 and exemplified in the case of 20°N by the Hovmöller diagram of tangential wind field shown in Fig. 5, we begin by examining the response of the boundary layer to such an expansion. To this end, we employ a simple, steady, slab boundary layer model as in SKM. The details of this model and the justification for its use are given in SKM. The use of this simple model is a key to breaking into the chain of coupled mechanisms referred to above. This is because the steady boundary layer equations on which the model is based are parabolic in the radially inward direction. Thus, the inflow and hence the ascent (or descent) at the top of the boundary layer at a given radius knows only about the tangential wind profile at larger radii: these flow features know nothing directly about the vertical motion in the MM5 calculation at the top of the boundary layer, including the pattern of ascent into the eyewall cloud associated with convection under the eyewall. In contrast, the MM5 does not solve the boundary layer equations separately, and it does not make any special boundary layer approximation. Thus, the ability of the slab boundary layer model to produce a radial distribution of vertical motion close to that in the

time-dependent MM5 provides a useful measure of the degree of boundary layer control in the evolution of the vortex.

For completeness, a brief summary of the slab boundary layer model is given in section 3 of SKM. For simplicity we assume here that the boundary layer has a constant depth of 1000 m, comparable to the depth of the layer of strong inflow in the MM5 simulation. We focus now on a comparison with the MM5 simulation for 20°N. The slab boundary layer calculations are performed every 12 h using the smoothed tangential wind profile extracted from the MM5 calculation shown in Fig. 5. Hovmöller diagrams of the radial and tangential velocity components u_b and v_b, respectively, and of the vertical velocity w_h at the top of the boundary layer for these solutions are compared with the corresponding diagrams from the MM5 simulation in Fig. 6. The radial and tangential wind components from the MM5 calculation are averaged over the lowest 1-km depth, corresponding to an average over the depth of the boundary layer, to provide a fair comparison with the slab boundary layer fields.

Despite the fact that the slab boundary layer calculations break down at some inner radius where the radial velocity tends to zero and the vertical velocity becomes large, they capture many important features of the corresponding depth-averaged boundary layer fields from the MM5 simulations. For example, they capture the broadening of the vortex core with time, that is, the increase of $R_{v\max}$, and eyewall location characterized by the location of maximum w_h. They capture also the broadening of the outer radial and tangential wind field. However, they overestimate the radial extent of the subsidence outside the eyewall (cf. Figs. 6e,f). For reasons articulated in the first paragraph of this section, these results provide strong support for the existence of a dynamical control by the boundary layer on the evolution of the vortex. There is a thermodynamic control also that we explore in the next subsection.

b. *Role of boundary layer thermodynamics and convective forcing*

The boundary layer is important not only in determining the location of the eyewall and the radial profiles of vertical velocity and tangential momentum entering the eyewall: it plays an important role in determining also the radial distribution of diabatic heating within the eyewall. The reason is that the wind field in the boundary layer affects the radial distribution of the surface enthalpy flux. In turn, this distribution is important because, in the context of axisymmetric balance dynamics, it is well known that diabatic heating associated with moist deep convection in the eyewall leads to inflow in the lower troposphere below the level of the heating maximum (Eliassen 1951; Willoughby 1979). Moreover, the strength of the inflow is related, inter alia, to the negative radial gradient of diabatic heating rate. This inflow draws M surfaces inward above the boundary layer where M is approximately conserved and is a central feature of the conventional spinup mechanism (Montgomery and Smith 2014).

We show in Fig. 7 Hovmöller diagrams of the time and azimuthally averaged diabatic heating rate in the MM5 simulations at a height of 6 km for all three experiments. Superimposed on these plots is the radius of the time and azimuthally averaged maximum vertical velocity at a height of 6 km. The distribution of the diabatic heating rate and its radial gradient weaken considerably with time at all latitudes. In particular, in all three experiments, the location of the maximum diabatic heating rate and the radius of maximum vertical velocity move radially outward with time. The outward movement of the maximum diabatic heating rate is expected from the boundary layer behavior described above. We explore the consequences of the changing heating rate for the calculation at 20°N in the next subsection. The latitudinal dependence is discussed in section 6.

c. *Diabatically forced balanced overturning circulation*

Following on from the foregoing description of the behavior of the diabatic heating rate, the question now is: can the expansion of the outer wind field in the MM5 calculation be explained by the temporal changes in the distribution of the diabatic heating rate? To answer this question, we adopt the approach of Bui et al. (2009) and solve the Sawyer–Eliassen (SE) equation for the secondary circulation forced by the distribution of azimuthally averaged diabatic heating rate derived from the MM5 output. The coefficients of this equation are determined by the azimuthally averaged tangential wind from the MM5 output and the corresponding balanced temperature field determined using the method described by Smith (2006). The tangential wind field and diabatic heating rates are time averaged over a 3-h period centered on intervals of 12 h from the initial time. In this section, we examine the results for the 20°N simulation.

The SE equation can be solved only if it remains elliptic at every grid point. If this is not the case, a regularization procedure must be carried out to restore the ellipticity at such grid points. Here we follow the ad hoc, but physically defensible, method suggested by Möller and Shapiro (2002), which is described in more detail by Bui et al. (2009).

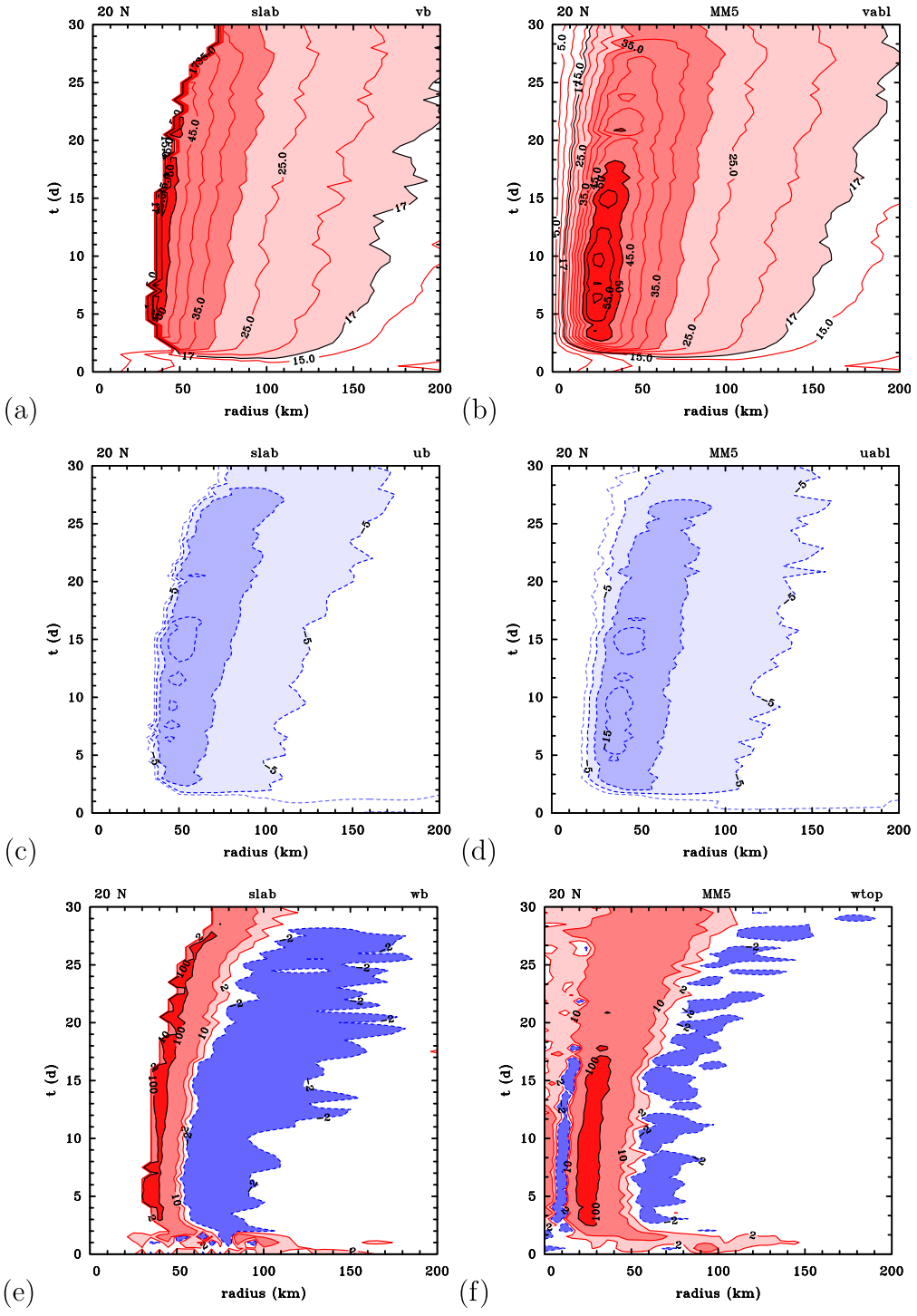

FIG. 6. (a),(c),(e) Azimuthally averaged and temporally smoothed Hovmöller plots of radial, tangential, and vertical velocities at the top of the boundary layer from the slab boundary layer model, with a constant depth of 1000 m for the experiment at 20°N. These calculations include only heat forcing and neglect frictional forcing. (b), (d),(f) The corresponding variables from the MM5 output. Contour intervals are as follows: (top) Contours are every 5 m s^{-1}. The 17 m s^{-1} contour representing the radius of gales is colored black. The interval from 17 to 30 m s^{-1} is shaded light red, that from 30 to 50 m s^{-1} is shaded slightly darker red, and values of 50 m s^{-1} and above are shaded dark red. (middle) First contour is -1 m s^{-1}, then in 5 m s^{-1} intervals. Light blue shading is from -5 to -10 m s^{-1}, with darker shading below -10 m s^{-1}. (bottom) First (red) contour is 2 cm s^{-1}, with light red shading up to 10 cm s^{-1} and darker shading from 10 to 100 cm s^{-1}. The darkest (red) shading is enclosed by a 100 cm s^{-1} black contour. Regions of downward motion are shaded blue and enclosed by a -2 cm s^{-1} blue contour. Solid (red) contours are positive, and dashed (blue) contours are negative.

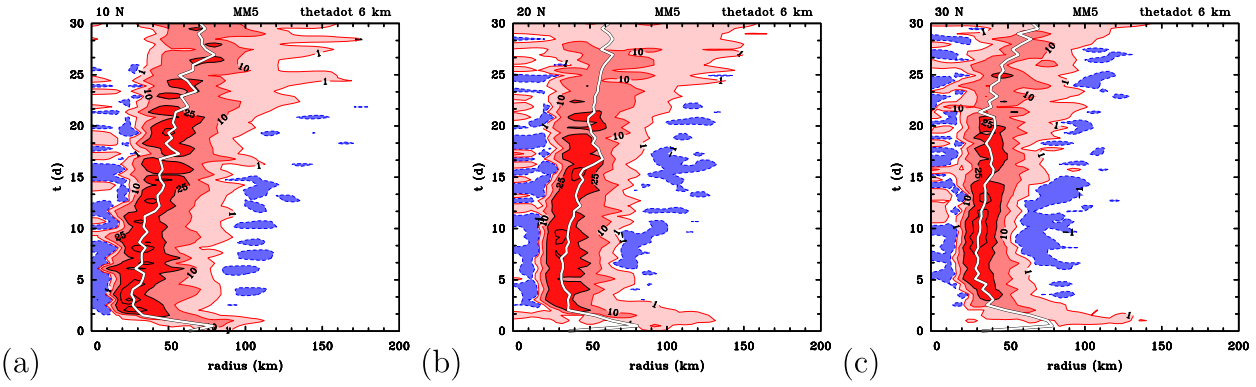

FIG. 7. Hovmöller plots of the azimuthally averaged and temporally smoothed diabatic heating rate in the MM5 simulations at a height of 6 km. Contour intervals are as follows: 1–10 K h^{-1} is shaded light red, and 10–25 K h^{-1} is shaded slightly darker red, and 25 K h^{-1} and above is shaded dark red with black contours every 25 K h^{-1}. Shaded blue regions are below −1 K h^{-1}. Solid (red) contours are positive, and dashed (blue) contours are negative. The white curve represents the radius of the time and azimuthally averaged maximum vertical velocity at a height of 6 km.

The SE equations are solved[3] with the diabatic heating rate at 20°N (see Fig. 7b), and Figs. 8a and 8c show Hovmöller plots of the Sawyer–Eliassen solutions for the radial and vertical wind fields at heights of 2.5 and 6 km, respectively. Figures 8b and 8d show the corresponding fields from the MM5 simulations. It is seen that the SE solutions broadly capture the magnitude and location of the eyewall updraft at a height of 6 km. There are differences in detail in that these solutions overestimate the inflow at a height of 2.5 km (Figs. 8c,d) as well as the horizontal extent of the region of subsidence (Figs. 8a,b). These differences would be consistent with the neglect of frictional effects in the SE calculation.

Figure 9 shows Hovmöller diagrams comparing the tangential wind tendencies at a height of 1.5 km in the balance calculation (excluding friction), in both cases evaluated as the sum of the radial flux of absolute vorticity and the vertical advective tendency. Shown also are R_{gales} (pink curve) and the $R_{w\max}$ (red curve) as a function of time. Broadly speaking, in the MM5 calculation, the tendency is largely positive both inside R_{gales} and outside, at least to the radius of 400 km shown. However, the positive tendency is interspersed by intervals of negative tendency that can be traced to bursts of outflow at this level associated with a temporal mismatch between the boundary layer convergence and the ventilation of this converging air by deep convection (not shown). The corresponding tendency in the SE calculation is entirely positive with values at and beyond R_{gales} increasing in strength with time. The lack of negative values is presumably attributed to the omission of friction effects in this calculation and the inability to capture the nonlinear dynamics of the corner flow region (Smith and Montgomery 2010).

d. Synthesis

In section 4a we showed that, forced by the radially expanding azimuthally averaged tangential wind field in the outer core from the MM5 calculation at the top of the boundary layer, a simple, steady, slab boundary layer predicts the radial expansion of the radial and tangential velocity components in the inner-core boundary layer as well as the vertical velocity at the top of the boundary layer. The radial expansion of the vertical velocity in the inner core accounts for an expansion of the distribution of diabatic heating rate in the free vortex (section 4b). In turn, we showed in section 4c that the balanced response of the vortex to the expanding azimuthally averaged diabatic heating rate diagnosed from the MM5 leads to an expansion of the inner-core tangential wind field at the top of the boundary layer. Taken together, these findings provide an explanation to the question posed in the title of the paper.

This study has presented a system-scale (azimuthally averaged) diagnostic analysis of vortex evolution. One notable question arises: How would the asymmetric eddies be expected to influence the new view developed here? The eddies as vortical hot towers play an important role, for example, by comprising the bulk of the azimuthal-mean heating rate during spinup. However, at later times when an annular eyewall emerges, the towers are highly strained, as discussed in Persing et al. (2013). It is not immediately a priori clear what role these eddies

[3] Specifically, we solve Eq. (14) of Bui et al. (2009), neglecting both frictional forcing and the relatively small contributions of the "eddy terms" as defined therein in this equation.

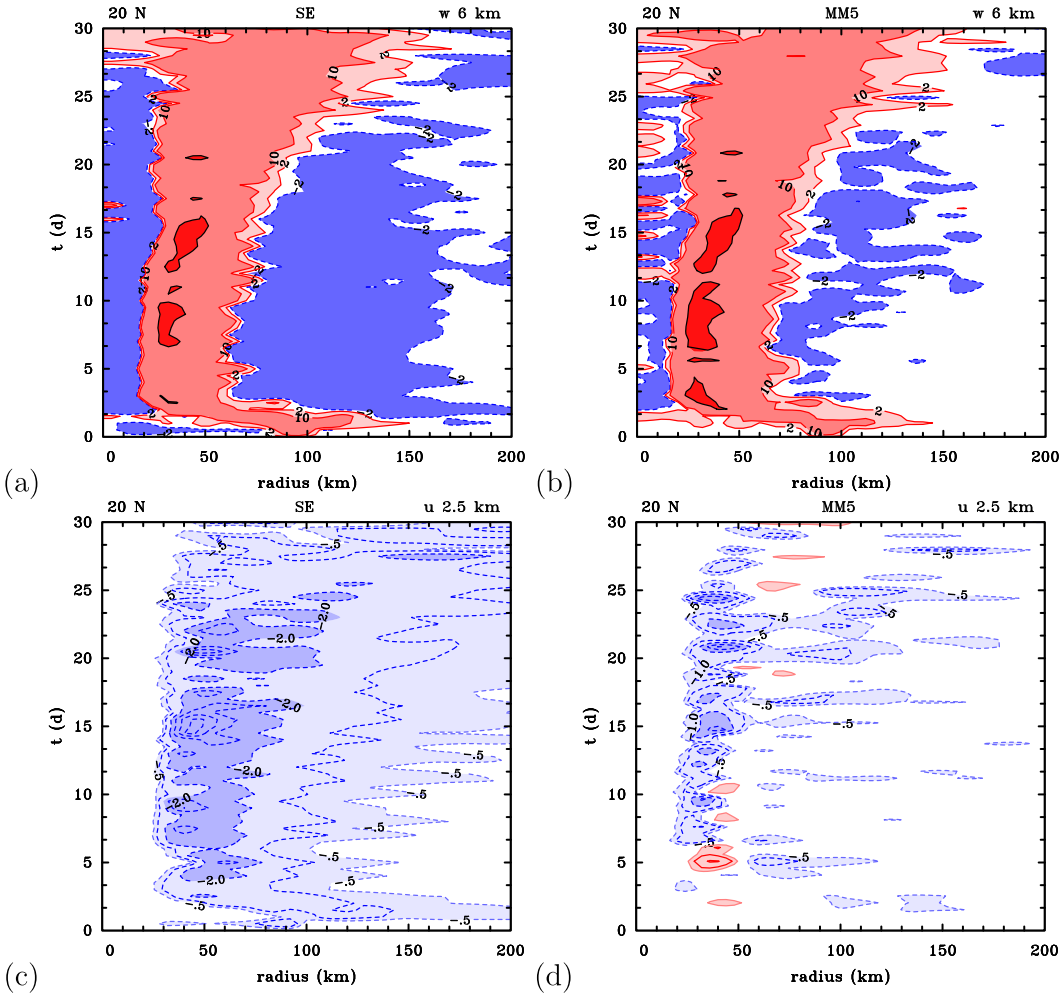

FIG. 8. (a),(c) Azimuthally averaged and temporally smoothed Hovmöller plots of radial and vertical velocities at a height of 2.5 km for radial velocity and a height of 6 km for vertical velocity from the balanced SE equation for the experiment at 20°N. These calculations include only heat forcing and neglect frictional forcing. (b),(d) The corresponding variables from the MM5 output. Contour intervals are as follows: (top) First (red) contour is 2 cm s^{-1}, with light red shading up to 10 cm s^{-1} and darker shading from 10 to 100 cm s^{-1}. The darkest (red) shading is enclosed by a 100 cm s^{-1} black contour. Regions of downward motion are enclosed by a −2 cm s^{-1} dashed blue contour and blue shading. (bottom) First contour is −0.5 m s^{-1} and then in intervals of 1 m s^{-1} from −1 m s^{-1}. Light shading is from −0.5 to −2 m s^{-1}, and darker shading is below −2 m s^{-1}. Solid (red) contours are positive, and dashed (blue) contours are negative. The red contours and shading in (d) are equal in magnitude but opposite in sign to the blue contours and shading.

play during the later expansion of the vortex. This is the topic of a future study.

5. An alternative explanation for size expansion in two notable tropical cyclones

The foregoing results concerning the outward migration of the tropical cyclone eyewall accompanied by the slowly declining maximum tangential winds provide new insight into observations of mature tropical cyclones. One well-documented storm that shared characteristics similar to these idealized numerical experiments was category 5 Atlantic Hurricane Isabel (2003). This hurricane was observed with multiple reconnaissance aircraft over three consecutive days. A summary of the inner-core, vortex-scale kinematic, dynamic, and thermodynamic structure of Isabel over these 3 days of observations was provided by Bell and Montgomery (2008). One particularly intriguing and unexplained feature of Hurricane Isabel's evolution over this period was the progressive lateral expansion of the eye region of the vortex (see Fig. 2 of Bell and Montgomery 2008). Figure 4 from that study shows that the expansion of the eye was accompanied by an expansion of the radius of maximum tangential wind $R_{v\max}$ and eyewall. In particular, $R_{v\max}$ grew from approximately 25 km on

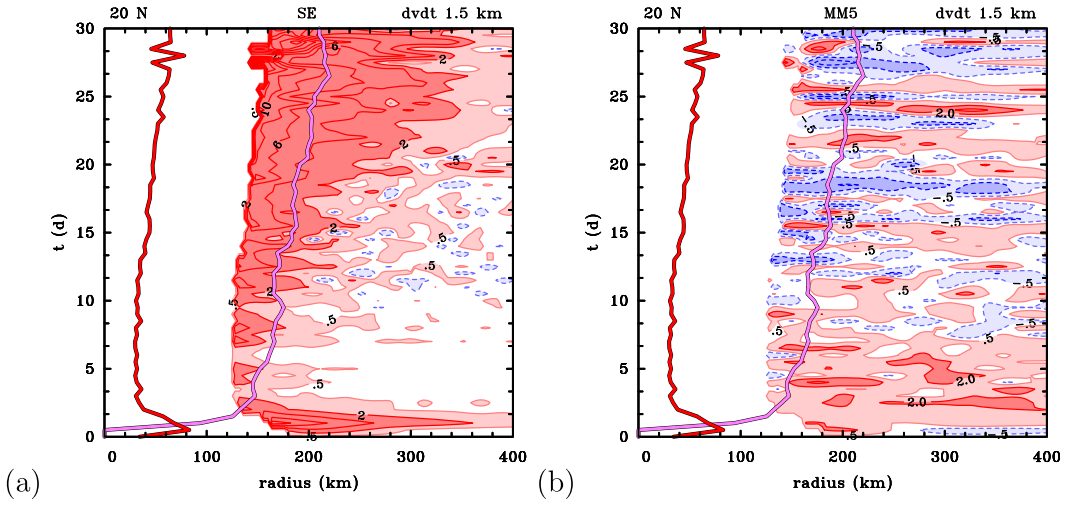

FIG. 9. Hovmöller diagrams comparing the azimuthally averaged and temporally smoothed tangential wind tendencies at a height of 1.5 km in the MM5 against the Sawyer–Eliassen balance calculation (excluding friction). Shown are the contributions outside 100 km of $R_{v\max}$ in order to focus attention on the outer core spinup. The figure shows also the time series of azimuthally averaged radius of gales at this level (pink curve) and the radius of maximum vertical winds (red curve). Contour intervals are as follows: from 0.5×10^{-5} to 2×10^{-5} m s^{-2} is in light red or blue shading, dark red or blue shading is above 2×10^{-5} m s^{-2}, and contours are in intervals of 2×10^{-5} m s^{-2} from 2×10^{-5} m s^{-2}. Positive tendencies are indicated by solid red contours and red shading; negative tendencies are indicated by dashed blue contours and blue shading.

12 September to 45 km on 13 September; $R_{v\max}$ continued to expand to 55 km on 14 September. During this extended observation interval, the maximum tangential wind declined slowly from approximately 80 to 74 m s^{-1}, still within category 5 status.

As discussed by Bell and Montgomery (their section 3a), one possible explanation for the expansion of the $R_{v\max}$ was an eyewall replacement cycle between 12 and 13 September. Radar reflectivity imagery and microwave imagery (their Fig. 2a) do suggest that an outer rainband began to encircle the primary eyewall late on 12 September. However, limited flight-level data and microwave imagery between the intensive observation periods preclude a definitive determination of an eyewall replacement event. The inner-core expansion mechanism discussed in the foregoing sections offers a plausible, and arguably simpler, explanation of Isabel's inner-core size expansion.

Another documented case of a storm that intensified rapidly with no eyewall contraction but a significant inner-core size increase was Typhoon Megi (2010). On the basis of a numerical simulation of this storm, Wang and Wang (2013, p. 65) proposed that "the inner-core size increase was primarily related to the binary interaction of Megi with a large-scale low-level depression in which Megi was embedded." They noted that "the shearing/merging of the large-scale depression with Megi and the subsequent axisymmetrization led to the strengthening of the outer circulation of Megi." As shown herein, this strengthening of the outer circulation would lead to a boundary layer response capable of explaining the inner-core size increase.

6. Dependence on latitude

The foregoing explanation for the progressive radial expansion of the vortex is based on a calculation for 20°N. Here we examine the latitudinal dependence of this intrinsic behavior. The results of SKM show that, for a moderately strong initial vortex ($V_{\max} = 15$ m s^{-1}), the boundary layer dynamics exert a significant control on the vortex spinup rate at a particular latitude. We see no reason to believe that this control should diminish in prominence as the vortex matures and decays. Another important factor is, of course, the strength of the convective forcing.

Some of the latitudinal behavior in the present calculations was shown in Figs. 1–4 and described in section 3. In particular, it was shown that during the initial period of contraction, as measured by $R_{v\max}$, the minimum value of $R_{v\max}$ decreases with latitude. As the vortices mature and decay, $R_{v\max}$ fluctuates in value, but the running mean increases as the difference between different latitudes declines.

During the first half of the simulations, in terms of either R_{gales} or R_{galesF}, the vortex size above the boundary layer increases with time at all three latitudes (Figs. 2a,b). The vortex at 10°N expands a little more

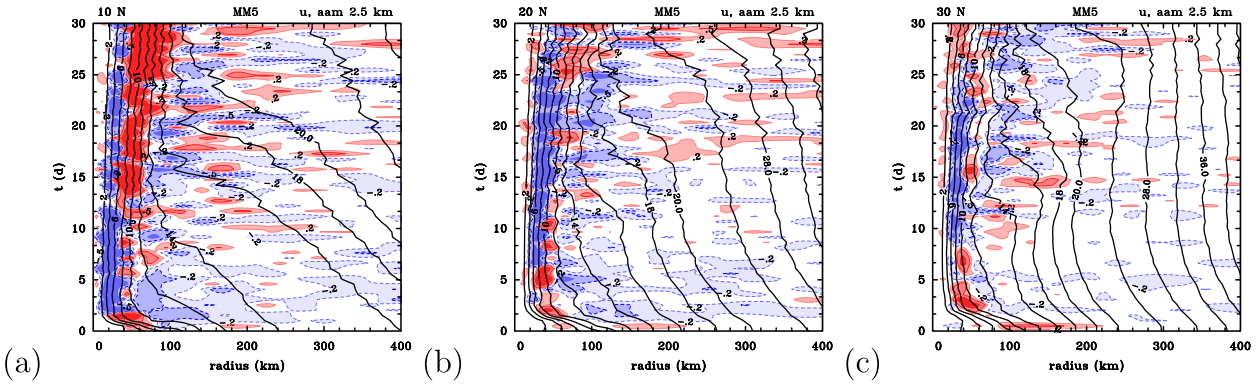

FIG. 10. Azimuthally averaged and temporally smoothed plots of AAM and radial velocity component at a height of 2.5 km for (a) 10°, (b) 20°, and (c) 30°N. Contour intervals are as follows: AAM is contoured in black from 2 $m^2 s^{-1}$ in intervals of 2 $m^2 s^{-1}$. Radial velocity contours are at 0.2 and 0.5 m s^{-1}. Light shading is between 0.2 and 0.5 m s^{-1}, and darker shading is above 0.5 m s^{-1}, with the darkest shading above 1 m s^{-1}. Solid (red) contours are positive, and dashed (blue) contours are negative; red shading is positive, and blue shading is negative.

slowly than those at 20° and 30°N, which have essentially the same size evolution. During the second half of the simulations, the vortices at 10° and 20°N grow in size together, while the size of the vortex at 30°N becomes approximately stationary, except for a small increase near the end of the simulation. The size values at a given time are not uniformly ordered with latitude on account of two competing effects. In the case of R_{gales}, these effects are the convectively driven inflow, which, because of changes in the distribution of diabatic heating in the lower troposphere, decreases in strength and radial extent as the latitude increases (Fig. 10), and the radial gradient of absolute angular momentum (AAM), which increases with latitude. It is not possible a priori to anticipate which effect will dominate: one must do the calculation to determine the outcome.

The time evolution of R_{galesF} is similar to that of R_{gales} (cf. Figs. 2a,b), but the latitudinal differences are smaller. In this case, the definition of R_{galesF} includes both the tangential and radial velocity components, and understanding its behavior requires consideration of the radial and tangential momentum equations, including friction. Again, one has to do the calculation to determine the outcome. Our calculations show that these competing effects nearly cancel, with only small differences in R_{galesF} between the different latitudes.

We showed in Fig. 3 that the strongest azimuthally averaged vertical motion occurs during the intensification phase, where it is notably larger at 10°N than at the higher latitudes. Thereafter, the peak values weaken with time, and there appears to be little systematic difference between them in the range of latitudes examined. In contrast, the area-averaged vertical mass flux carried by the azimuthal-mean eyewall updraft exhibits rapid temporal fluctuations with time, but the running mean increases monotonically with time, both at 1.5 and 6 km (Fig. 4). At a particular time, the mass flux is smaller when the latitude is increased. Figure 11 shows the difference in a running time average over 12 h of the corresponding mass flux curves in Fig. 4 between 6 and 1.5 km, expressed as a percentage of the mass flux at 1.5 km. During the rapid intensification phase (approximately 1–6 days depending on latitude), when the convection is most vigorous (Fig. 3a), there is adequate ventilation of the air that exits the boundary layer at all latitudes in the sense that the mass flux at 6-km height exceeds that at 1.5 km.

As the vortices mature (approximately during the period 3–9 days, depending on latitude), the boundary layer upflow slightly exceeds the mass flux at 6 km, again at all latitudes. This behavior is accompanied by a progressive warming of the upper levels (not shown), which

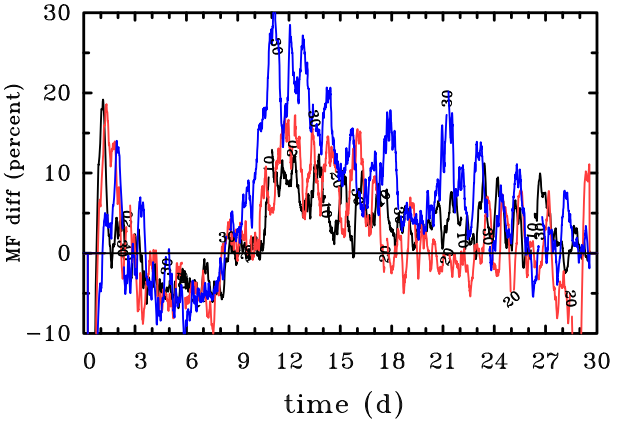

FIG. 11. Normalized mass flux difference between 6 and 1.5 km for 10°–30°N. The difference is calculated as a running time average over 12 h of the corresponding mass flux curves in Fig. 4 between 6 and 1.5 km and then expressed as a percentage of the mass flux at 1.5 km.

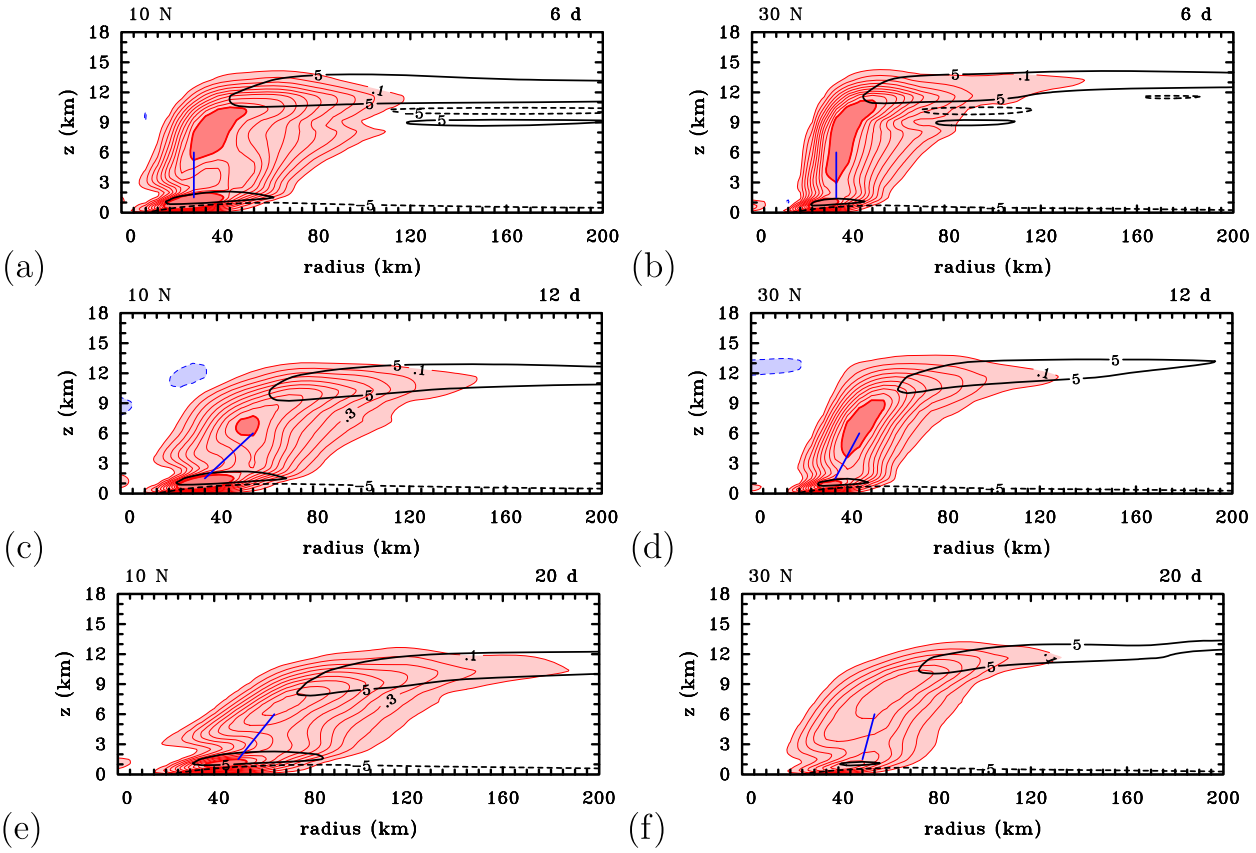

FIG. 12. Vertical cross sections of the azimuthally averaged, 24-h time-averaged vertical velocity and radial velocity at (a),(c),(e) 10° and (b),(d),(f) 30°N. Contour intervals are as follows: Contours 0.1–0.9 m s^{-1} are enclosed by light shading. A thick contour above 1 m s^{-1} encloses an area of darker shading. Regions of downward motion are shaded blue, and those of upward motion are shaded red. The black contours show regions of strong radial inflow and outflow, greater than 5 m s^{-1}. Solid contours are positive; dashed contours are negative. Shown also is the slope of the eyewall in the lower troposphere (blue line), characterized by the difference in radial location of w_{max} between heights of 1.5 and 6 km.

reduces the convective instability in the inner-core region, as is evident in the progressive decline in maximum azimuthally averaged vertical velocity. Despite the reduced convective instability, the increase in the mass flux at 6 km beyond the intensification phase is accompanied by an outward radial displacement of the azimuthal-mean eyewall updraft as well as a broadening of the updraft. During the decay phase (beyond about 9 days), the mass flux at a height at 6 km once again exceeds that at 1.5 km and is accompanied by a continued structural change in the eyewall.

The structural evolution of the eyewall updraft referred to above is illustrated in Fig. 12, which shows vertical cross sections of the azimuthally averaged vertical velocity in the calculations at 10° and 30°N at selected times. Shown also is the 5 m s^{-1} contour of radial velocity and the slope of the eyewall in the lower troposphere, characterized by the difference in radial location of w_{max} between heights of 1.5 and 6 km. At 6 days, when the two vortices have reached maturity, the eyewall updraft is upright at both latitudes; but, in comparing the details of these figures, one should recall that the vortex at 30°N reaches maturity three days later than that at 10°N. A prominent difference between the two simulations is the more inward penetration of the boundary layer inflow at the lower latitude and the correspondingly larger region of outflow just above the inflow layer. This more extensive outflow at 10°N appears to influence the radial location and extent of the updraft at all levels.

As time proceeds, the updrafts at both latitudes continue to broaden as the pattern of upflow at the top of the boundary layer broadens (Fig. 13) and the maximum vertical velocity aloft weakens (Fig. 12). This broadening is accompanied by a progressively increasing outward tilt of the updraft as indicated in Fig. 12. Moreover, the positive ventilation implied by the larger mass flux at a height of 6 km than at 1.5 km is accompanied

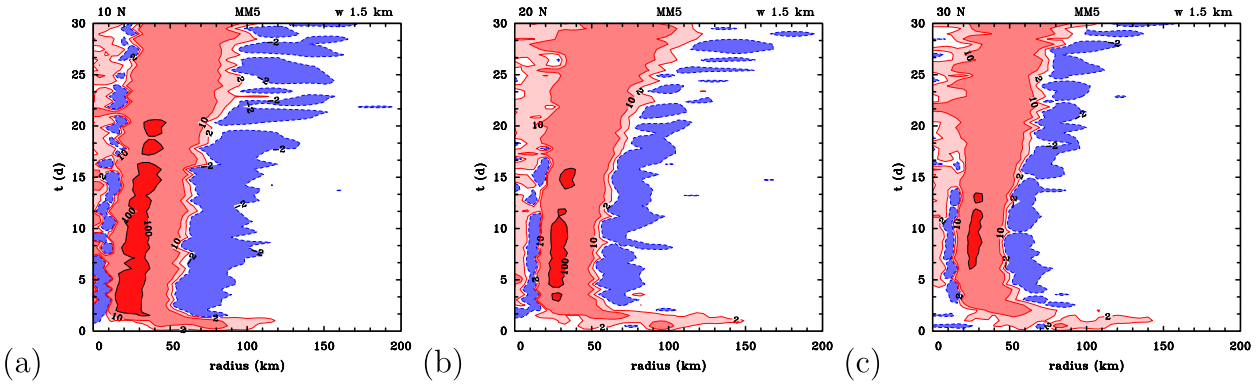

FIG. 13. Hovmöller plots of the vertical velocity in the MM5 simulations at a height of 1.5 km. Contour intervals are as follows: First (red) contour is 2 cm s^{-1}, with light red shading up to 10 cm s^{-1} and darker shading from 10 to 100 cm s^{-1}. The darkest (red) shading is enclosed by a 100 cm s^{-1} black contour. Regions of downward motion are shaded blue and enclosed by a -2 cm s^{-1} blue contour. Solid (red) contours are positive, and dashed (blue) contours are negative.

by (mostly) entrainment into the updraft at outer radii as seen in the Hovmöller diagram of inflow and the radially inward slope of the M surfaces at a height of 2.5 km in Fig. 10. A consequence of this inflow is a continued expansion of the outer tangential wind field in the lower troposphere. Note that, at 30°N, the M surfaces at 2.5-km height beyond a radius of about 300 km and after about 15 days are no longer moving inward, indicating that the outer wind field has ceased to expand, consistent with the behavior of R_{gales} at this latitude in Fig. 2a.

In summary, the purpose of this section was to describe and interpret the variability of tropical cyclone life cycle with latitude in a quiescent environment. We have shown that, at all latitudes, the tangential wind field in the free troposphere progressively broadens on account of inflow associated with deep convection in the eyewall updraft, except at 30°N, where the broadening declines after about 15 days. The inflow is consistent through mass continuity with the excess mass flux in the eyewall updraft at a height of 6 km compared with that at a height of 1.5 km during the decay stage of the vortices. The convective mass fluxes, both at 6 and 1.5 km, increase with decreasing latitude, a feature that may be attributed to the strength of the boundary layer control on the eyewall updraft, which increases also with decreasing latitude. In brief, the boundary layer affects the location and radial extent of the eyewall updraft as well as the radial gradient of θ_e exiting the boundary layer into the updraft. As shown above and in SKM, these features of the boundary layer depend both on the radial distribution of tangential wind at the top of the boundary layer as well as on latitude. Because of the tight coupling between the boundary layer and the tangential wind field at its top, it is not possible, a priori, to make a prediction about which effect will win: one has to do the calculation.

7. Conclusions

We have examined the long-term (out to 30 days) behavior of tropical cyclones in the prototype problem for cyclone intensification on an f plane using a nonhydrostatic, three-dimensional numerical model. We showed that the model cyclones grow progressively in size and decay in intensity after reaching their mature stage. As they decay, the inner-core size, characterized by the radius of the eyewall, and size of the outer circulation, characterized for example by the radius of gale-force winds, both progressively increase, except at latitude 30°N where the radius of gales tends to become steady. The strongest vertical motion occurs during the intensification phase and weakens with time, while the location of the strongest vertical motion moves radially outward with time at all latitudes studied. The evolution of vertical mass flux carried by the eyewall updraft depends also on latitude.

We answer the question posed in the title of the paper by isolating what might be described as a set of coupled mechanisms, the first of which we refer to as a boundary layer control mechanism. We showed that, forced by the radially expanding azimuthally averaged tangential wind field in the outer core from the numerical model simulation at the top of the boundary layer, a simple, steady, slab boundary layer model correctly predicts the radial expansion of the radial and tangential velocity components in the inner-core boundary layer as well as the vertical velocity at the top of the boundary layer. The radial expansion of the vertical velocity in the inner core accounts for an expansion of the distribution of

diabatic heating rate in the free vortex. In turn, we showed that the balanced response of the vortex to the expanding azimuthally averaged diabatic heating rate diagnosed from the numerical model leads to an expansion of the inner-core tangential wind field at the top of the boundary layer. Taken together, these findings provide an explanation to the question posed in the title of the paper. They provide also a plausible, and arguably simpler, explanation for the expansion of the inner core of Hurricane Isabel (2003) and Typhoon Megi (2010) during and after peak intensity than given previously.

Finally, we showed that both the strength of the boundary layer control on the location and radial extent of the eyewall updraft, as well as the thermodynamic control of the boundary layer on the distribution of diabatic heating in the updraft, have a latitudinal dependence. Since the distribution of diabatic heating determines primarily the strength of the secondary circulation, it has an indirect effect on the radial distribution of tangential wind at the top of the boundary layer, which therefore has a latitudinal dependence as well. Because of the tight coupling between the boundary layer and the tangential wind field above the boundary layer, which is itself determined by the diabatic heating, it is not possible to make an a priori prediction of how the vortex evolution will change with latitude: one has to do the calculation.

Acknowledgments. We thank Dr. Christoph Schmidt for his perceptive comments on an earlier version of the manuscript. We thank also Noel Davidson and two anonymous reviewers for their thoughtful comments on the original version of the manuscript. RKS and GK acknowledge financial support for this research from the German Research Council (Deutsche Forschungsgemeinschaft) under Grant SM30-23 and the Office of Naval Research Global under Grant N62909-15-1-N021. MTM acknowledges the support of Interagency Agreement NSF AGS-1313, NOAA HFIP Grant N0017315WR00048, NASA Grant NNG11PK021, and the U.S. Naval Postgraduate School. The views expressed herein are those of the authors and do not represent sponsoring agencies or institutions.

REFERENCES

Bell, M. M., and M. T. Montgomery, 2008: Observed structure, evolution, and potential intensity of category 5 Hurricane Isabel (2003) from 12 to 14 September. *Mon. Wea. Rev.*, **136**, 2023–2046, doi:10.1175/2007MWR1858.1.

Beven, J. L., and Coauthors, 2008: Atlantic hurricane season of 2005. *Mon. Wea. Rev.*, **136**, 1109–1173, doi:10.1175/2007MWR2074.1.

Bui, H. H., R. K. Smith, M. T. Montgomery, and J. Peng, 2009: Balanced and unbalanced aspects of tropical cyclone intensification. *Quart. J. Roy. Meteor. Soc.*, **135**, 1715–1731, doi:10.1002/qj.502.

Chan, K. T. F., and J. C. L. Chan, 2015: Impacts of vortex intensity and outer winds on tropical cyclone size. *Quart. J. Roy. Meteor. Soc.*, **141**, 525–537, doi:10.1002/qj.2374.

Chavas, D. R., and K. Emanuel, 2014: Equilibrium tropical cyclone size in an idealized state of axisymmetric radiative convective equilibrium. *J. Atmos. Sci.*, **71**, 1663–1680, doi:10.1175/JAS-D-13-0155.1.

Davidson, N. E., 2010: On the intensification and recurvature of Tropical Cyclone Tracy (1974). *Aust. Meteor. Oceanogr. J.*, **60**, 169–177.

Dean, L., K. A. Emanuel, and D. R. Chavas, 2009: On the size distribution of Atlantic tropical cyclones. *Geophys. Res. Lett.*, **36**, L14803, doi:10.1029/2009GL039051.

DeMaria, M., and J. D. Pickle, 1988: A simplified system of equations for simulation of tropical cyclones. *J. Atmos. Sci.*, **45**, 1542–1554, doi:10.1175/1520-0469(1988)045<1542:ASSOEF>2.0.CO;2.

Dunnavan, G. M., and J. W. Diercks, 1980: An analysis of Super Typhoon Tip (October 1979). *Mon. Wea. Rev.*, **108**, 1915–1923, doi:10.1175/1520-0493(1980)108<1915:AAOSTT>2.0.CO;2.

Eliassen, A., 1951: Slow thermally or frictionally controlled meridional circulation in a circular vortex. *Astrophys. Norv.*, **5**, 19–60.

Emanuel, K. A., 2004: Tropical cyclone energetics and structure. *Atmospheric Turbulence and Mesoscale Meteorology: Scientific Research Inspired by Doug Lilly*, E. Fedorovich, R. Rotunno, and B. Stevens, Eds., Cambridge University Press, 165–192.

Frisius, T., 2015: What controls the size of a tropical cyclone? Investigations with an axisymmetric model. *Quart. J. Roy. Meteor. Soc.*, **141**, 2457–2470, doi:10.1002/qj.2537.

Fudeyasu, H., and Y. Wang, 2011: Balanced contribution to the intensification of a tropical cyclone simulated in TCM4: Outer-core spinup process. *J. Atmos. Sci.*, **68**, 430–449, doi:10.1175/2010JAS3523.1.

Grell, G. A., J. Dudhia, and D. R. Stauffer, 1995: A description of the fifth-generation Penn State/NCAR Mesoscale Model (MM5). NCAR Tech. Note NCAR/TN-398+STR, 121 pp. [Available online at http://nldr.library.ucar.edu/repository/assets/technotes/TECH-NOTE-000-000-000-214.pdf.]

Hakim, G. J., 2011: The mean state of axisymmetric hurricanes in statistical equilibrium. *J. Atmos. Sci.*, **68**, 1364–1376, doi:10.1175/2010JAS3644.1.

Kepert, J. D., 2006a: Observed boundary layer wind structure and balance in the hurricane core. Part I: Hurricane Georges. *J. Atmos. Sci.*, **63**, 2169–2193, doi:10.1175/JAS3745.1.

——, 2006b: Observed boundary layer wind structure and balance in the hurricane core. Part II: Hurricane Mitch. *J. Atmos. Sci.*, **63**, 2194–2211, doi:10.1175/JAS3746.1.

Li, T., X. Ge, M. Peng, and W. Wang, 2012: Dependence of tropical cyclone intensification on the Coriolis parameter. *Trop. Cyclone Res. Rev.*, **1**, 242–253.

Lussier, L. L., B. Rutherford, M. T. Montgomery, M. A. Boothe, and T. J. Dunkerton, 2015: Examining the roles of the easterly wave critical layer and vorticity accretion during the tropical cyclogenesis of Hurricane Sandy. *Mon. Wea. Rev.*, **143**, 1703–1722, doi:10.1175/MWR-D-14-00001.1.

Mapes, B. E., and P. Zuidema, 1996: Radiative–dynamical consequences of dry tongues in the tropical troposphere. *J. Atmos. Sci.*, **53**, 620–638, doi:10.1175/1520-0469(1996)053<0620:RDCODT>2.0.CO;2.

Merrill, R. T., 1984: A comparison of large and small tropical cyclones. *Mon. Wea. Rev.*, **112**, 1408–1418, doi:10.1175/1520-0493(1984)112<1408:ACOLAS>2.0.CO;2.

Möller, J. D., and L. J. Shapiro, 2002: Balanced contributions to the intensification of Hurricane Opal as diagnosed from a GFDL model forecast. *Mon. Wea. Rev.*, **130**, 1866–1881, doi:10.1175/1520-0493(2002)130<1866:BCTTIO>2.0.CO;2.

Montgomery, M. T., and R. K. Smith, 2014: Paradigms for tropical cyclone intensification. *Aust. Meteor. Oceanogr. J.*, **64**, 37–66. [Available online at http://www.bom.gov.au/amoj/docs/2014/montgomery_hres.pdf.]

——, M. E. Nichols, T. A. Cram, and A. B. Saunders, 2006: A vortical hot tower route to tropical cyclogenesis. *J. Atmos. Sci.*, **63**, 355–386, doi:10.1175/JAS3604.1.

——, J. Persing, and R. K. Smith, 2014: Putting to rest WISHE-ful misconceptions for tropical cyclone intensification. *J. Adv. Model. Earth Syst.*, **7**, 92–109, doi:10.1002/2014MS000362.

Nguyen, V. S., R. K. Smith, and M. T. Montgomery, 2008: Tropical-cyclone intensification and predictability in three dimensions. *Quart. J. Roy. Meteor. Soc.*, **134**, 563–582, doi:10.1002/qj.235.

Persing, J., M. T. Montgomery, J. McWilliams, and R. K. Smith, 2013: Asymmetric and axisymmetric dynamics of tropical cyclones. *Atmos. Chem. Phys.*, **13**, 12 299–12 341, doi:10.5194/acp-13-12299-2013.

Rappin, E. D., M. C. Morgan, and G. J. Tripoli, 2011: The impact of outflow environment on tropical cyclone intensification and structure. *J. Atmos. Sci.*, **68**, 177–194, doi:10.1175/2009JAS2970.1.

Rotunno, R., and K. A. Emanuel, 1987: An air–sea interaction theory for tropical cyclones. Part II: Evolutionary study using a nonhydrostatic axisymmetric numerical model. *J. Atmos. Sci.*, **44**, 542–561, doi:10.1175/1520-0469(1987)044<0542:AAITFT>2.0.CO;2.

Sanger, N. T., M. T. Montgomery, R. K. Smith, and M. M. Bell, 2014: An observational study of tropical cyclone spinup in Supertyphoon Jangmi (2008) from 24 to 27 September. *Mon. Wea. Rev.*, **142**, 3–28, doi:10.1175/MWR-D-12-00306.1.

Smith, R. K., 2006: Accurate determination of a balanced axisymmetric vortex in a compressible atmosphere. *Tellus*, **58A**, 98–103, doi:10.1111/j.1600-0870.2006.00149.x.

——, and M. T. Montgomery, 2010: Hurricane boundary-layer theory. *Quart. J. Roy. Meteor. Soc.*, **136**, 1665–1670, doi:10.1002/qj.679.

——, C. W. Schmidt, and M. T. Montgomery, 2011: Dynamical constraints on the intensity and size of tropical cyclones. *Quart. J. Roy. Meteor. Soc.*, **137**, 1841–1855, doi:10.1002/qj.862.

——, M. T. Montgomery, and J. Persing, 2014: On steady-state tropical cyclones. *Quart. J. Roy. Meteor. Soc.*, **140**, 2638–2649, doi:10.1002/qj.2329.

——, G. Kilroy, and M. T. Montgomery, 2015: Why do model tropical cyclones intensify more rapidly at low latitudes? *J. Atmos. Sci.*, **72**, 1783–1804, doi:10.1175/JAS-D-14-0044.1.

Wang, Y., and H. Wang, 2013: The inner-core size increase of Typhoon Megi (2010) during its rapid intensification phase. *Trop. Cyclone Res. Rev.*, **2**, 65–80, doi:10.6057/2013TCRR02.01.

Willoughby, H. E., 1979: Forced secondary circulations in hurricanes. *J. Geophys. Res.*, **84**, 3173–3183, doi:10.1029/JC084iC06p03173.

Xu, J., and Y. Wang, 2010: Sensitivity of tropical cyclone inner-core size and intensity to the radial distribution of surface entropy flux. *J. Atmos. Sci.*, **67**, 1831–1852, doi:10.1175/2010JAS3387.1.

Yamasaki, M., 1968: Numerical simulation of tropical cyclone development with the use of primitive equations. *J. Meteor. Soc. Japan*, **46**, 178–201.